

STATISTICAL ANALYSIS OF BATSE GAMMA-RAY BURSTS:  
SELF-SIMILARITY AND THE AMATI-RELATIONL. BORGONOVO<sup>1</sup> AND C. -I. BJÖRNSSON<sup>1</sup>  
Stockholm Observatory, SE-10691 Stockholm, Sweden*To appear in ApJ – Version Date: October 14, 2018*

## ABSTRACT

The statistical properties of a complete, flux limited sample of 197 long gamma-ray bursts (GRBs) detected by BATSE are studied. In order to bring forth their main characteristics, care was taken to define a representative set of ten parameters. A multivariate analysis gives that  $\sim 70\%$  of the total variation in parameter values is driven by only three principal components. The variation of the temporal parameters is clearly distinct from that of the spectral ones. A close correlation is found between the half-width of the autocorrelation function ( $\tau$ ) and the emission time ( $T_{50}$ ); most importantly, this correlation is self-similar in the sense that the mean values and dispersions of both  $\tau$  and  $T_{50}$  scale with the duration of the burst ( $T_{90}$ ). It is shown that the Amati-relation can be derived from the sample and that the scatter around this relation is correlated with the value of  $\tau$ . Hence,  $\tau$  has a role similar to that of the break in the afterglow light curve ( $t_b$ ) in the Ghirlanda-relation. In the standard GRB-scenario, the close relation between a global parameter ( $t_b$ ) and a local one ( $\tau$ ) indicates that some of the jet-properties do not vary much for different lines of sight. Finally, it is argued that the basic temporal and spectral properties are associated with individual pulses, while the overall properties of a burst is determined mainly by the number of pulses.

*Subject headings:* gamma rays: bursts – gamma rays: observations – methods: data analysis

## 1. INTRODUCTION

The Burst and Transient Source Experiment (BATSE) collected during its operation the most extensive gamma-ray burst (GRB) database to the present day, with more than 2700 triggered bursts. Even with the advent of *Swift* and the future mission *GLAST*, it will remain the most complete burst catalog for many years to come. With such a wealth of data, there are many statistical techniques that could be used to investigate the sample characteristics. So far this analysis has focused mainly on bivariate methods. Such an approach has some drawbacks for intrinsic relations involving more than two observables, since the analysis is limited to two dimensional projections of the actual relation. Not only do such projections increase the scatter but, most importantly, selection effects and observational biases can, for example, introduce spurious correlations. Hence, multivariate methods are to be preferred when the quality of the data is such that this can be reliably done. In the present work a principal component analysis (PCA) is performed on a complete, flux limited sample of GRBs chosen from the BATSE database. Alternative multivariate methods have been discussed and used by Mukherjee et al. (1998) in connection with attempt to discriminate between distinct classes of GRBs.

The PCA is a well-known statistical tool, widely used in many scientific disciplines. Some areas of astronomy, like the study of active galactic nuclei and quasi-stellar objects, have long benefited from this technique (e.g., by Boroson & Green 1992; Boroson 2002). The method finds, in decreasing order, orthogonal directions of maximal variation. The most common use of the PCA is to reduce the number of variables needed to reproduce the variability of the data without essential loss of information. Since in most practical situations there is a significant amount of inter-correlation among the observed quantities, there is then some degree of redundancy in the multi-dimensional data. This simplifies the data analysis, for example, when looking for subclasses. Previous uses of the PCA in the field of GRBs (e.g., by Bagoly et al. 1998;

Balázs et al. 2003) were done mainly for this purpose. However, the PCA can also be an important aid to better understand the generally complex correlation structure encountered in multivariate studies and to gain physical insight to the system under study. It is with this purpose in mind that we have selected a broader range of physical parameters for our sample of GRBs than the ones considered in previous works. We include various basic temporal and spectral parameters in order to characterize temporal variability and spectral evolution.

Throughout this paper only long GRBs will be considered (i.e., those with time duration  $> 2$  s) since short bursts need to be treated separately. This is not only because they are most likely a different physical class, but also because it would not be possible to derive for them some of the parameters under consideration, which are already hard to measure for the long bursts. The characterization of the temporal properties is complicated by the remarkable morphological diversity of GRBs light curves and the presence of long emission *gaps* in a significant fraction of them. Hence, a parameter designed to give a measure of some property for a “typical” GRB light curve will often fail to give consistent or physically meaningful results in other cases. The problem extends to any other temporally averaged property which follows the pulse structure of the light curve. For this reason, seemingly similar measures of a given property but based on different criteria can have a complementary roll, as it will be shown in this work.

The paper is organized as follows. In § 2 we present the sample and discuss the motivation for the choice of parameters used in the subsequent analysis. A short introduction to PCA is given in § 3. Special attention is given to the estimate of uncertainties in the coefficients of the principal components; in particular, the effects of mixing and reordering of the principal components due to (nearly) degenerate eigenvalues are discussed. The basic statistical results are presented in § 4, where also a brief discussion is given of how they compare to previous studies. A more in depth analysis is done in § 5, where it is shown that two redshift independent correla-

tions can be derived from the data. One of the challenges of statistical studies is to distinguish between direct causal connections and those due to association through some common variable not necessarily included in the analysis. In an attempt to make the overall correlation structure of the parameters more distinct, we develop a new method in § 5.3, in which ranking of correlations is combined with the PCA. It is shown that this reveals considerably more structure than does, for example, the use of only the ranking of correlations. Finally, in § 6 we discuss our results with a particular emphasis on how they can be used together with results already established to illuminate some of the basic properties of GRBs.

## 2. DATA

### 2.1. Burst Data - Sample Selection

The present work is based on data taken by BATSE on board the *Compton Gamma-Ray Observatory* (CGRO; Fishman et al. 1989) that operated between the years 1991–2000. It consisted of eight modules placed on each corner of the satellite, giving full sky coverage. Each module had two types of detectors: the Large Area Detector (LAD) and the Spectroscopy Detector (SD). The former had a larger collecting area and is suited for spectral continuum studies, while the latter was designed for the search of spectral features (lines). The *CGRO* Science Support Center (GROSSC) supplies a number of high-level data products in its public archive. For our spectral analysis we used primarily the high energy resolution (HER) background and burst data types from the LADs having 128 energy channels in the 20–2000 keV energy band summed from triggered detectors, and a time-resolution of multiples of 64 ms. For long and bright bursts it is often the case that the recorded HER data are incomplete, however for the bright cases we were able to use the Spectroscopy High Energy Resolution Burst (SHERB) data obtained with the SDs. These detectors had better energy resolution (256 energy channels) in the same energy band, but given their smaller collecting area, the signal-to-noise ratio (S/N) is often too low for time resolved spectral analysis. If that was the case, we used alternatively the Medium Energy Resolution (MER) data that consist of 16-channel spectra. When possible, comparisons of the best-fit parameters using these three data formats were made, and the results were consistent within uncertainties (see also Preece et al. 2000).

For the temporal analysis we used the so-called concatenated 64 ms burst data, which is a concatenation of the three standard BATSE data types DISCLA, PREB, and DISCSC. All three data types have four energy channels (approximately 25–55, 55–110, 110–320, and  $> 320$  keV). The DISCLA data is a continuous stream of 1.024 s and the PREB data covers the 2.048 s prior to the trigger time at 64 ms resolution, both types obtained from the 8 LADs.

To construct our sample, we first selected from the Current BATSE Catalog all bursts with time duration  $T_{90} \geq 2$  s and a peak flux measured within the 1.024 s time scale  $F_{1s} \geq 4$  photons  $\text{cm}^{-2}\text{s}^{-1}$  in the 50–300 keV energy band. A few cases (11) were not suitable for our analysis due to, e.g., data gaps, poor background information, or missing data formats, leaving a total sample of 197 bursts.

### 2.2. Parameter Selection

In order to characterize the total time of activity of a burst different criteria can be adopted. The most commonly used in the literature is  $T_{90}$ , the time interval within which 5%

to 95% of the total count fluence has been detected. Similarly  $T_{50}$  measures the interval during which 50% of the total counts have been observed. In general, these two quantities are highly correlated, but the second is sometimes preferred when studying “weak” bursts as a more robust measure, but this difference is not relevant for our sample. We used values taken from the BATSE catalog.

Since a significant fraction of bursts show quiet intervals or *gaps* in their time histories, other complementary parameters have been proposed to estimate the emission time scale. We use the emission time  $\mathcal{T}_n$  as defined by Mitrofanov et al. (1999), which is the smallest time interval that contains a given percentage  $n\%$  of the total count fluence. Again, 50% and 90% are the most commonly used percentile values, and we choose here  $\mathcal{T}_{50}$  since it is *less* correlated with  $T_{90}$  (i.e., it provides less redundant information). To calculate it, first the bins of the (background-subtracted) count time history are sorted by intensity. Then, starting from the largest intensity bin,  $\mathcal{T}_{50}$  is the integration time needed to accumulate 50% of the total counts.

We considered various parameters related to the temporal variability of GRBs that have been previously used in the literature. The parameter used here is the half-width at half-maximum of the autocorrelation function (ACF), which will be denoted by  $\tau$ , and it was calculated in the 50–300 keV energy band following Borgonovo (2004). In the context of GRBs, where most light curves show multiple uncorrelated pulses,  $\tau$  gives a measure of the typical pulse time-scale.

A dimensionless variability parameter, calculated in the local frame of the burst, was proposed by Reichart et al. (2001) as a possible “Cepheid-like” parameter that would correlate with the burst luminosity (though see Guidorzi et al. 2005, for a critical analysis of this claim). Since, in the present analysis, we are considering the *observed* characteristics of the bursts (i.e., at redshift  $z = 0$ ), we will adopt a somewhat simplified version of that given by Reichart et al. (2001). For a uniformly sampled light curve, let  $c_i$  be the net count level at bin  $i$ , and  $b_i$  the corresponding background level. The variability  $V$  is then defined as

$$V = \frac{\langle \sum[(c_i - s_i)^2 - (c_i + b_i)] \rangle}{\sum c_i^2} \quad (1)$$

where  $s_i$  is the corresponding value of the *smoothed* light curve using a boxcar function with a width given by the emission time at the 45% level,  $\mathcal{T}_{45}$ . Thus, the parameter is a measure of the variability content at high frequencies. Subtracting the gross detected counts in the numerator takes into account the Poisson noise contribution, while the sum in the denominator is used for normalization. Alternatively, we could have used the square of the number of counts at the peak of the light curve,  $F_{pk}^2$ , as first proposed in Fenimore & Ramirez-Ruiz (2000). In a recent study Li & Paczyński (2006) found a better variability-luminosity correlation using the  $F_{pk}^2$  normalization, although they also introduced a different filtering method. Initially we considered both options, but in our case the latter choice shows similar though weaker correlations. Therefore, we will only present the results obtained from the variability definition given in equation (1). The percentile level of the smoothing time-scale  $\mathcal{T}_{45}$  was determined by Reichart et al. (2001) to render the best results in their variability-luminosity correlation studies, which gives an additional motivation for the inclusion of the nearly identical  $\mathcal{T}_{50}$  in our analysis.

TABLE 1  
STATISTIC DESCRIPTION OF BURST PARAMETERS

Parameter	Median	QD	Min	Max	$\sigma(\log x)$	K-S test	G test
$T_{90}(\text{s})$	31.2	22.7	2.24	674.	0.48	0.42	0.57
$T_{50}(\text{s})$	4.67	3.63	0.256	32.6	0.44	0.11	0.03
$\tau(\text{s})$	3.12	2.81	0.144	39.2	0.49	0.70	0.29
$V$	0.0039	0.0030	0.000084	0.029	0.49	0.018	0.32
$S_{\mathcal{F}}$	1.49	1.33	0.086	57.3	0.52	0.29	0.34
$\tau_{\text{lag}}(\text{s})$	0.053	0.034	0.001	2.70	0.51	0.0002	0.0003
$\mathcal{R}E_{\text{pk}}$	1.36	0.40	0.40	6.05	0.17	0.005	0.42
$\mathcal{F}(10^6 \text{ erg cm}^{-2})$	35.3	35.0	1.70	781.	0.54	0.31	0.18
$E_{\text{pk}}(\text{keV})$	351.	146.	70.	2251.	0.28	0.76	0.11
$\alpha$	-0.59	0.27	-1.59	1.49	—	0.001	$< 10^{-5}$

The emission strength of the bursts is usually characterized by either its peak count flux in a given time interval or its energy fluence, both directly available from the BATSE catalog. Since the peak flux  $F_{1s}$  has been used for our sample selection, its observed distribution is more limited and biased than in the fluence case. Restricted to the sample range, the peak flux shows weak or no significant correlation with the other parameters considered in our PCA, with the exception of the fluence. For this reason in the presented PCA we will only include the total energy fluence  $\mathcal{F}$ . Fluence values discriminated by energy channel were first considered but they do not show significant differences. In their correlation analysis, Bagoly et al. (1998) found the fluence from the fourth energy channel ( $> 300 \text{ keV}$ ) to be individually a significant principal component. Note, however, that their sample comprise both short and long bursts. When considering long bursts, only the principal component given by the sum of all energy channels was found to be significant, i.e., the fourth channel fluence discriminates between the two well-known soft/long and hard/short classes but does not stand out within each class.

To characterize the GRBs spectral shape we modeled the photon spectrum with the standard GRB function (Band et al. 1993), which is a softly broken power-law. This empirical function has four free parameters; namely, the amplitude, the peak energy  $E_{\text{pk}}$  at which the  $EF_{\text{E}}$ -spectrum is at its maximum, and the low and high asymptotic power-law indices  $\alpha$  and  $\beta$ . Unfortunately, in general the high-energy index  $\beta$  is poorly constrained, and often it has to be fixed to allow the convergence of the modeling algorithm. Hence, we included in our study only the spectral parameters  $E_{\text{pk}}$  and  $\alpha$ . Since all long GRBs show a significant spectral evolution, initially we considered both time integrated spectra over the whole burst and time-resolved spectra at the time  $t_{\text{max}}$  when the light curve reaches its maximum. Note that because we required a  $S/N \geq 40$  to allow a reliable spectral deconvolution with the detector response, the time resolution at the light curve peak varies for different bursts, but it is typically of  $\sim 128 \text{ ms}$ . The spectral parameters measured for the two cases are highly correlated. Since the correlations with the other variables were strongest for the  $t_{\text{max}}$ -case, only this case is included in our study.

Except for the simple bursts with a single long smooth pulse, where the characteristic energy  $E_{\text{pk}}$  changes monotonically from hard to soft, most bursts show a very complex spectral evolution that correlates with the pulse structure (see, e.g., Borgonovo & Ryde 2001). To have a simple measure of the overall change, we first divided the burst light curve into two fluence-halves, from 5–50% and 50–95% of the total

counts, and then determined the individual integrated spectra for each of the two time intervals. We defined the ratio  $\mathcal{R}E_{\text{pk}} = E_{\text{pk}}^{(1)}/E_{\text{pk}}^{(2)}$ , so that  $\mathcal{R}E_{\text{pk}} > 1$  implies an overall hard to soft evolution. The difference between the  $\alpha$ -values for each fluence-half was initially also considered, but in general the estimated changes were not very significant when compared with the large  $\alpha$  uncertainties. This results in a very noisy parameter that only shows weak correlations with the others, and it was therefore excluded. From the division in two fluence-halves we can derive another related parameter by considering the ratio between the corresponding time intervals. Thus, we define the *emission symmetry* as  $S_{\mathcal{F}} = T_2/T_1$  so that  $S_{\mathcal{F}} > 1$  implies an overall decay of the intensity on the pulses, or in the case of single-pulse bursts, a fast rise and slow decay. Note that by definition it follows that  $T_{90} = T_1 + T_2$ . The two new parameters  $\mathcal{R}E_{\text{pk}}$  and  $S_{\mathcal{F}}$  have obviously the important property of being, at least to first order, redshift independent.

A more commonly used parameter related to the spectral evolution of the bursts is the time-lag between two energy channels, derived from the analysis of the cross-correlation function (CCF). Following Norris (2002), we define the time-lag,  $\tau_{\text{lag}}$ , as the time at which the CCF reaches its maximum. Among all possible CCFs between the different energy channels, we consider here only the one between the third and the first ( $CCF_{31}$ ) that gives the best S/N (Norris et al. 2000). Note that the parameters  $\mathcal{R}E_{\text{pk}}$  and  $\tau_{\text{lag}}$  are in principle complementary, since they are related to the spectral changes on long and short time-scales, respectively. Therefore, in general, the first is a measure of the overall spectral evolution and the other of the evolution within a pulse.

In summary, from all the GRBs parameters considered in this section, we have selected 10 for multivariate analysis, describing a broad range of temporal and spectral characteristics. They are the following: duration time  $T_{90}$ , emission time  $T_{50}$ , ACF half-width  $\tau$ , variability  $V$ , emission symmetry  $S_{\mathcal{F}}$ ,  $CCF_{31}$  time lag  $\tau_{\text{lag}}$ , the ratio of peak energies  $\mathcal{R}E_{\text{pk}}$ , fluence  $\mathcal{F}$ , peak energy  $E_{\text{pk}}$ , and low energy spectral index  $\alpha$ .

### 3. METHOD

For a data set with  $n$  variables, the most basic way to analyze the multidimensional structure of the correlations between all the variables is to organize the linear correlation coefficients  $R$  between all possible pairs of variables in matrix form, i.e., to construct a *correlation matrix*. However, unless the resulting matrix is very simple or the number of variables very small, usually not much direct information will be gained by this approach. Various methods have therefore been de-

veloped with the aim to simplify the problem enough for the main characteristics of the data to become discernible. The principal component method achieves this essentially by diagonalizing the correlation matrix and consequently provides a new set of uncorrelated variables (called principal components, PCs) associated with the simplest possible matrix correlation structure (i.e., the diagonal form).

Principal component analysis (PCA) is a widely used technique in multivariate analysis. By definition, the first PC gives the direction of maximal variance. The second PC gives the direction of the second highest variance orthogonal to the first PC, and so forth. It has been shown (see, e.g., Jolliffe 2002) that the computation of the PCs reduces to the problem of finding the eigenvectors and eigenvalues of the correlation matrix derived from the original variables, where the eigenvalues give the variance associated with each PC. Real number solutions are ensured by the matrix symmetry. The PCs are then sorted in decreasing eigenvalue order, so that each PC has associated a decreasing percent of the total variability, given by the  $n$ -dimensional variance of the sample. They are usually defined with unity norm so that, except for an arbitrary sign, they are uniquely determined. In theory, this is not generally true since there could be degenerate eigenvalues, but this situation is extremely unlikely when dealing with experimental data. However, the existence of very similar eigenvalues can have practical consequences, as we will discuss later in connection to the uncertainty estimations.

By construction, every PC is a linear combination of the  $n$  original variables  $x_j$

$$PC_i = \sum_{j=1}^n a_{ij} x_j \quad (2)$$

where the coefficients  $a_{ij}$  are sometimes referred to as *loadings* since they represent how much each variable  $x_j$  contributes to a given  $PC_i$ . By definition, the *matrix of coefficients*  $\mathbf{A} \equiv (a_{ij})_{n \times n}$  transforms the data points expressed in the vector space basis comprised by the original variables  $x_j$  to the  $PC_i$  basis, and it is obtained by arranging the  $n$  eigenvectors of the correlation matrix in columns. Consequently, each row in  $\mathbf{A}$  is associated with one PC and each column with one of the original variables.

The PC representation has many advantages, and it is most commonly used to reduce the number of variables needed to describe the data. Since the first PCs retain most of the variability of the data, we could then discard the last PCs without significant loss of information. Various criteria have been proposed to decide how many PCs should be reasonably kept. Once the number of variables are reduced to a few, the analysis of the data and their graphical representation are greatly simplified (e.g., when looking for subclasses or *clusters*, and classification). A complementary aspect of the PCA is that it can be used to find near-constant linear relationships between the variables when the last PCs have small associated eigenvalues (and therefore very small associated variances). In those cases, the interpretation of the last PCs is consequently much more direct than that of the first PCs, and it can often be of considerable interest and provide constraints on physical models.

We will use the logarithms of the variables defined in § 2.2 since the distribution of most of our variables are well described by log-normal distributions (see, e.g., Preece et al. 2000, and § 4.1 below) and taken into consideration that most of the inference based on PCA assumes a multivariate

normal distribution (Jolliffe 2002). Thus, unless stated otherwise, throughout this paper we will speak about *linear* correlations but between *logarithmic* variables. The only variables in our set that are not positive by definition are  $\alpha$  and  $\tau_{\text{lag}}$ . For the low energy index, we considered both the direct value of  $\alpha$  and the simple transform  $\log(\alpha+2)$  since  $\alpha+2 > 0$  for all  $\alpha$ , but the results were very similar, and only the first option will be presented. In the lag case, 3 points in our sample have near-zero negative values, but within errors they can be taken as intrinsically positive. For a much larger sample, Norris (2002) also found that the lower tail of the lag distribution reaches negative values, but he has shown that the observations are consistent with the assumption that all GRB lags are positive, and the few exceptions are produced by measurement uncertainties. We considered both the use of  $\log \tau_{\text{lag}}$  with the exclusion of the 3 negative points, or the adoption of positive values within uncertainties ( $1\sigma$ ), with almost identical results. The last option was chosen for the present analysis.

To estimate the uncertainties of the PC coefficients we used the *bootstrap* method (see, e.g., Press et al. 1992) which does not rely on any assumptions of the distributions. However, the use of this method in the PCA is not straightforward. To obtain meaningful results, for each generated surrogate sample, care must be taken both to prevent sign switching (since they are arbitrary) and reordering of the PCs. The last problem occurs when two eigenvalues are equal to within uncertainties. This situation will often produce a switch in order, but, in practice, it may act also as a degeneracy where linear combinations of the two PCs could result. For this purpose, our code implementation of the bootstrap method compares the original matrix of coefficients  $\mathbf{A}$  with each bootstrap realization  $\mathbf{B}$ . By construction  $\mathbf{A}$  is orthonormal, i.e., the product with its transposed is  $\mathbf{A}\mathbf{A}' = \mathbf{I}$ , where  $\mathbf{I}$  is the identity matrix. Similarly, the product matrix  $\mathbf{C} = \mathbf{AB}'$  has most elements in each row nearly zero, and one element (or more in case of degeneracy) approximately  $\pm 1$ . After identification of the extreme elements in each  $\mathbf{C}$  row, the PCs in  $\mathbf{B}$  are reordered and switched given a new matrix  $\mathbf{B}_{\text{sort}}$  such that  $\mathbf{AB}'_{\text{sort}} \simeq \mathbf{I}$ . Finally, the  $\mathbf{A}$  uncertainties are estimated by calculating the sample standard deviation of the generated set  $\{\mathbf{B}_{\text{sort}}\}$ .

## 4. STATISTICAL RESULTS

### 4.1. Statistical Description of Burst Parameters

In Table 1 we present basic statistics of the burst parameters based on our sample of 197 GRBs. The first two columns show the median and the quartile deviation (QD). Since most parameters have approximately log-normal distributions, they are robust estimators of the typical values and dispersions. The ranges are given in the next two columns showing the minimum and maximum values. For later reference, we show in the fifth column the standard deviations  $\sigma$  of the logarithm of each given parameter. We tested the observed distributions for log-normality using the Kolmogorov-Smirnov (K-S) test which is a standard statistical test to compare any two distributions (e.g., Press et al. 1992), and the Geary (G) test which is specifically designed to test the normality distribution case (Devore 1982). The last two columns list the estimated probabilities. Note that since we derived from the sample the mean and dispersion parameters of the analytical log-normal distribution, the K-S test probabilities had to be estimated from Monte Carlo simulations. Variables like  $T_{90}$ ,  $\tau$ , and  $S_{\mathcal{F}}$  seem well described by the log-normal distribution, while for  $\tau_{\text{lag}}$  and  $\alpha$  it is likely a poor approximation. Nevertheless, in all cases it provides better fits than the normal distribution.

Some of these GRBs parameters have been extensively studied in the literature (see references in § 2.2). This is certainly the case for  $T_{90}$ ,  $T_{50}$ ,  $\mathcal{F}$ ,  $E_{\text{pk}}$ , and  $\alpha$ . The ranges and distributions observed in our GRB sample are consistent with the ones derived in these earlier works for long GRBs. The only exception is the bias towards larger fluences  $\mathcal{F}$  due to our selection criteria. For the new ( $\mathcal{S}_{\mathcal{F}}$  and  $\mathcal{R}E_{\text{pk}}$ ) or the less studied ( $\tau$ ,  $V$ , and  $\tau_{\text{lag}}$ ) burst parameters, we show in Figure 1 their respective probability density functions (PDFs) and cumulative distribution functions (CDFs). The latter are compared with the best-fit log-normal distribution (*dashed lines*).

#### 4.2. Correlation Matrix

In Table 2 we show the correlation matrix for our set of 10 variables. For a sample of 197 bursts, the correlation coefficients  $R = 0.18, 0.23, 0.27$  have a probability of chance occurrence  $p = 0.01, 0.001, 0.0001$  respectively. We estimated uncertainties using the *bootstrap* method. The correlation matrix shows few strong correlations, and many weak but significant. As always, it should be remembered that correlation coefficients are often sensitive to observational biases and selection effects. When the actual correlation involves more than two variables forming, e.g., a planar distribution of the data points in a multidimensional space, the result of a bivariate analysis depends on how these data points are distributed in that plane. In contrast, the normal to that plane is rather insensitive to the actual distribution of points so long as the thickness of the plane is much smaller than its extent. In spite of these limitations we include here a few comments on the correlation coefficients as presented in Table 2. This is done in order to compare our results with those of previous work.

The strongest correlation coefficient  $R$  is between  $T_{50}$  and  $\tau$  with  $R_{[\log T_{50}, \log \tau]} = 0.87$ . Naturally, the correlations between these two and the rest of the parameters are very similar; however, it is important to notice the differences that appear in the relation with the other two temporal parameters  $T_{90}$  and  $V$ , with  $T_{50}$  showing significantly stronger correlations in both cases. The fluence  $\mathcal{F}$  strongly correlates with the temporal parameters. These fluence correlations have been reported earlier in studies of the BATSE catalog, and they are only slightly increased here by our sample selection. With our selection criteria, the lower threshold of the fluence depends on the duration and, hence, there is a detection bias against weak and long bursts. It is difficult at this stage to determine how much of the correlation is produced by this bias; however, in an analysis of the fluence truncation effects Lee & Petrosian (1997) concluded that it is mainly intrinsic (see also Mukherjee et al. 1998; Balázs et al. 2003). The observed correlation between  $\mathcal{F}$  and  $E_{\text{pk}}$  is equally well-known, and it was also shown to be primarily of intrinsic origin (Mallozzi et al. 1995; Lloyd et al. 2000). A least-squares fit gives  $E_{\text{pk}} \propto \mathcal{F}^{0.29 \pm 0.03}$  in full agreement with the index  $0.28 \pm 0.04$  found by Lloyd et al. (2000).

The newly defined parameters, the emission symmetry  $\mathcal{S}_{\mathcal{F}}$  and the peak energy ratio  $\mathcal{R}E_{\text{pk}}$ , show a significant correlation. Such a correlation is expected in simple bursts with FRED-like (fast-rise slow-decay) structure due to the observed hard to soft evolution during the decay phase (Borgonovo & Ryde 2001). Hence, this correlation indicates that the more FRED-like is the light curve the better is the hardness-intensity correlation. These new parameters also show an anti-correlation with the variability  $V$ , that is further discussed in § 5.1. There seems to be only a weak correlation between the two spectral-evolution parameters  $\mathcal{R}E_{\text{pk}}$  and  $\tau_{\text{lag}}$ . The  $\tau_{\text{lag}}$  also correlates weakly with  $(-)E_{\text{pk}}$  and  $\alpha$ , and it ap-

pears to be independent of the other parameters. Norris et al. (2000) found, for a small sample of GRBs with known redshift, an anti-correlation between peak luminosity  $L$  and lag  $\tau'_{\text{lag}}$  calculated in the local frame. However, as the authors noted, in the observer's frame there is neither an apparent correlation between peak flux  $F$  and lag  $\tau_{\text{lag}}$  (we calculated for our sample  $R_{[\log F, \log \tau_{\text{lag}}]} = 0.004$ ), nor between fluence and lag (see Table 2). In order to verify that our result is consistent with that of Norris et al. (2000), we used the observed sample of lags  $\tau_{\text{lag}}$  together with redshifts for 37 pre-*Swift* GRBs and the bootstrap method to randomly draw surrogate data. We then generated realizations of the lag-flux data sample by applying the power-law relation derived for  $L(\tau')$  by Norris et al. (2000), adding noise to reproduce the observed dispersion. Taking into account the sample flux range, no significant correlation was obtained in agreement with the observations. We find a weak correlation between  $\mathcal{F}$  and  $V$ , which is probably a consequence of the correlation between  $\mathcal{F}$  and  $T_{50}$  (as we will show later in § 5.3) and most likely has no relation with the luminosity-variability correlation claimed by Reichart et al. (2001) since for our sample  $R_{[\log F, \log V]} = 0.01$ . We also find an anti-correlation between  $V$  and  $\tau_{\text{lag}}$ , as reported by Schaefer et al. (2001). The low-energy power-law index  $\alpha$  shows only weak correlations. The known anti-correlation between  $\alpha$  and  $E_{\text{pk}}$ , although here hardly significant considering the uncertainties, has been explained as a fitting artifact (see, e.g., Preece et al. 1998; Lloyd & Petrosian 2000).

#### 4.3. Principal Components

From the correlation matrix shown in Table 2, we derive the matrix of coefficients  $\mathbf{A}$  (defined in eq. [2]) that describes the linear transformation of the initial variables into the basis of PCs. In Table 3 the  $i$ -th data row corresponds to the  $PC_i$  indicated in the first column. The coefficients  $a_{ij}$  from equation (2) that determine the PCs are given in columns 2–11, where each column is associated with one of the variables in Table 2. The last two columns show the percentage of total variation,  $Var$ , and the cumulative percentage of variation,  $CVar$ .

To estimate the corresponding uncertainties we used the implementation of the bootstrap method described in § 3, which takes care of possible re-ordering and sign switching of the PCs. Nevertheless, some degree of “mixing” cannot be prevented when two eigenvalues are equal to within uncertainties. That is the case between  $PC_5$  and  $PC_6$ , where the errors are consequently overestimated (i.e., the shown uncertainties should be taken as upper limits). On the other hand,  $PC_1$  and  $PC_{10}$  are examples of “stable”, well-determined principal components. Additional degeneracy may exist in subspaces associated with subsets of variables that are closely interrelated (e.g., the subset of temporal variables). Unusually large uncertainties in some coefficients within a PC are likely due to this problem.

As we explained in § 3, one of the PCA applications is the derivation of a reduced set of variables to describe the data. Adopting the conservative criterion given by Jolliffe (2002), for a set of  $n$  variables, the number  $m$  of PCs needed to reproduce the observe variation of the data is given by those PCs with more than  $(70/n)\%$  percentage of variation. In the present case  $n = 10$ , so looking at the percentage of variation  $Var$  in Table 3, a rejection level of 7% gives  $m = 5$ . This suggests retaining the first 5 PCs, although the last two are marginal. The implications of these PCs are discussed in more

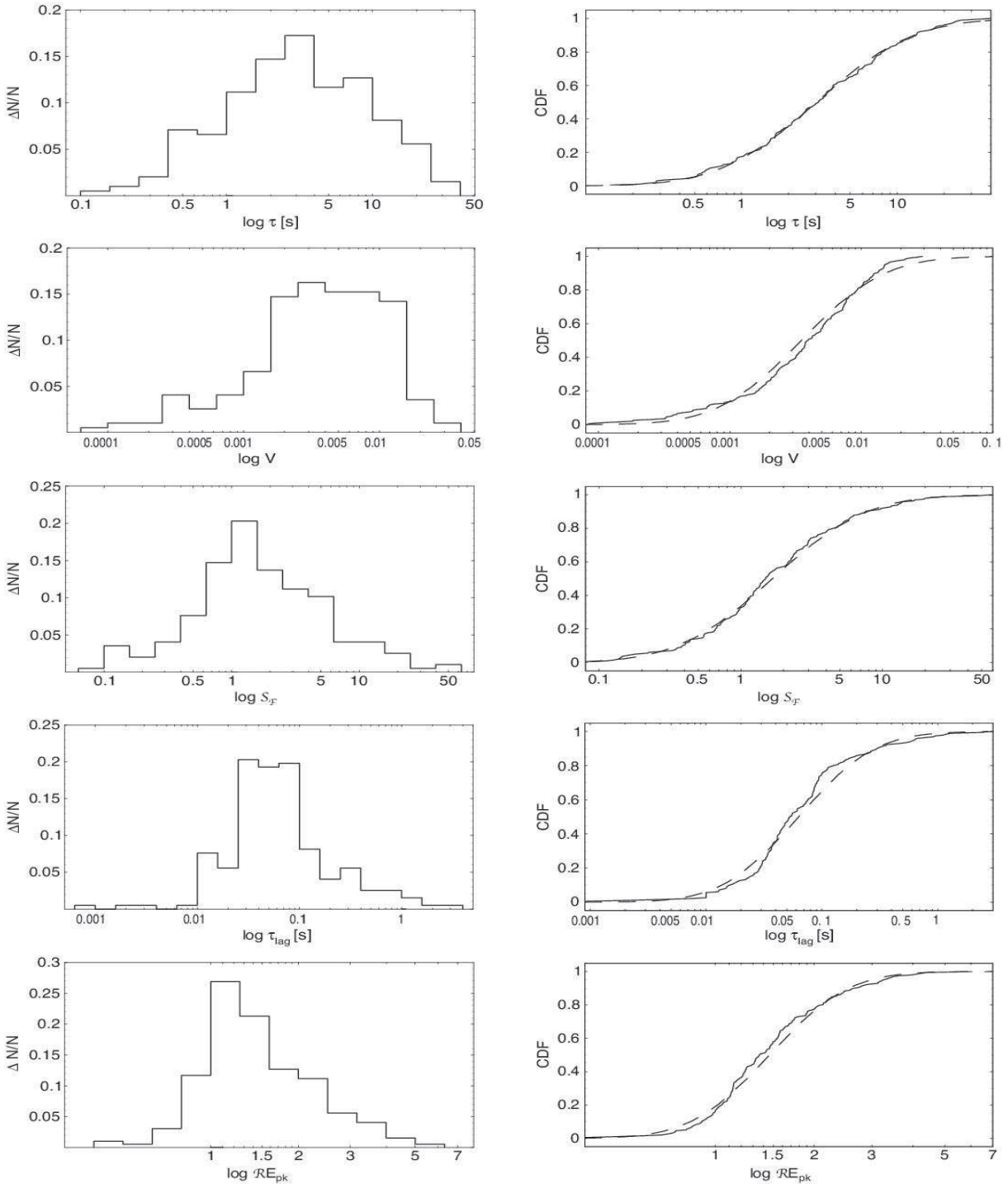


FIG. 1.— Probability density functions (PDFs) and cumulative distribution functions (CDFs) for five of the burst parameters included in our analysis (i.e., the autocorrelation function (ACF) half-width at half-maximum  $\tau$ , the variability  $V$ , the emission symmetry  $S_F$ , the time lag  $\tau_{\text{lag}}$ , and the peak energy ratio  $\mathcal{R}E_{\text{pk}}$ ). In the CDFs we show for comparison both the observed distribution (solid lines) and the analytical log-normal distribution that best describes it (dashed lines). Very good fits are obtained for the logarithms of  $\tau$  and  $S_F$  (see Table 1 for the results of comparative statistical tests). Note that the newly define parameters  $S_F$  and  $\mathcal{R}E_{\text{pk}}$  are in most cases (but not always) larger than unity implying, according with their definitions, that for most bursts there is an overall flux decay and hard-to-soft evolution.

detail later in § 5.3. Instead we will start with the analysis of the PCs with the smallest eigenvalues, which have a more direct physical interpretation.

## 5. ANALYSIS

All burst parameters are subjected to some degree of observational bias. This can have many causes like the sensitivity limit of the instrument, its energy band, the temporal resolution of the light curves, etc. As mentioned above such biases together with the selection criteria can sometimes significantly distort the observed relation between two param-

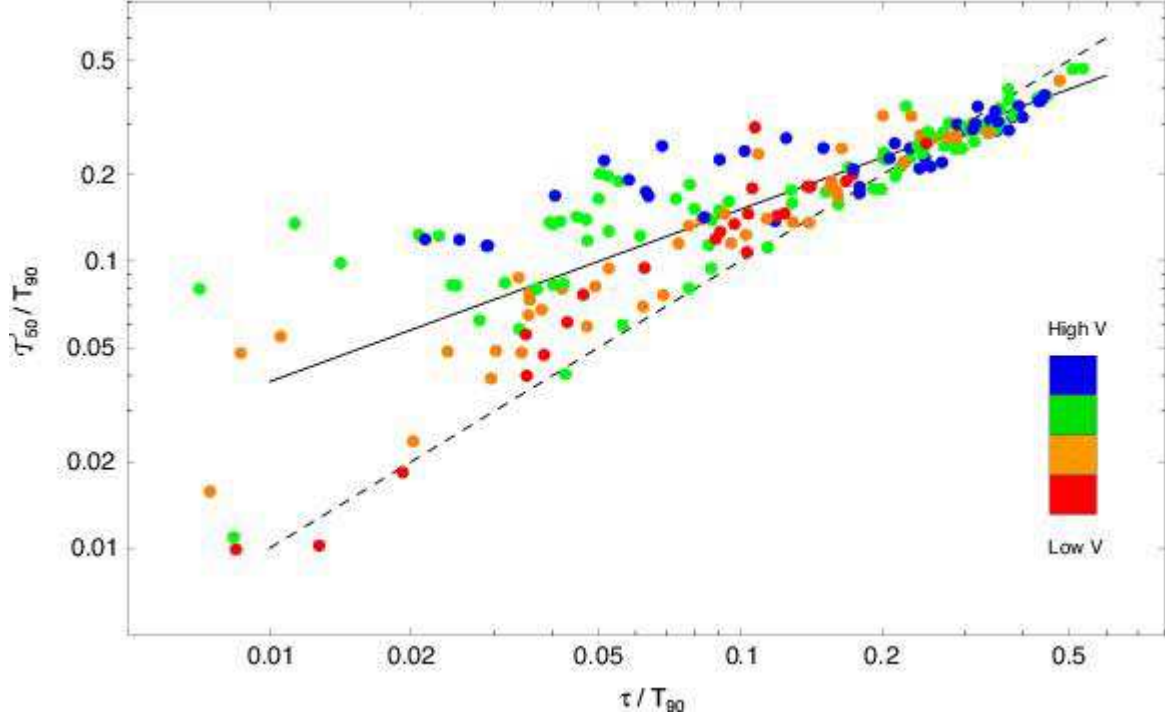


FIG. 2.— Relation between four temporal variables: duration time  $T_{90}$ , emission time  $T_{50}$ , half-width at half-maximum of the autocorrelation function  $\tau$ , and high frequency variability  $V$  (bluish and reddish dots indicate high and low variability values, respectively). The data points are distributed in an angular sector where the lower limit is given approximately by the identity relation (dashed line). A power-law fit of the data (solid line) gives an index  $0.60 \pm 0.03$  in agreement with equation (4).

eters and generate false correlations. In contrast, the directions of the PCs with the smallest eigenvalues (see § 3) are more robust against systematic errors. Even if a threshold in one of the parameters cuts off part of the sub-space orthogonal to such a PC, or a bias affects the way points are distributed within that sub-space, the orientation of the sub-space is unlikely to be substantially affected. Hence, analytical constraints imposed on the variations of parameters from PCs with small eigenvalues are expected to be rather insensitive to biases and selection effects.

### 5.1. $T_{90}$ - $T_{50}$ - $\tau$ Correlation

The last PC has associated with it a very small percentage of the total variation, with  $Var \simeq 0.5\%$ . For this reason  $PC_{10}$  represents a nearly constant relation between the few variables with significantly large loadings, i.e., the temporal variables  $T_{90}$ ,  $T_{50}$ , and  $\tau$ . Taking into account that the coefficients in Table 3 give the linear combination of the logarithms of the original variables, normalized by their standard deviations  $\sigma$ , it follows

$$T_{90}^{0.36} T_{50}^{-0.79} \tau^{0.45} \simeq \text{const.}, \quad (3)$$

where the  $\sigma$ -values were taken from Table 1. Then equation (3) can be approximately rewritten as

$$(T_{50}/T_{90}) \propto (\tau/T_{90})^{0.6}, \quad (4)$$

so that the duration of the burst can be used as normalization. The main thing to notice from equation (4) is the indication of a *self-similar* structure of the GRB light curves. This is a non-trivial property; two of the exponents in equation (3) are independent and, hence, it is in general not possible to arrange three PCA parameters in this way. It is also clear that this is an *intrinsic* property, since the ratios in equation (4) do not depend on redshift. We should also remark that the measure  $\tau$  in

long burst light curves is at least several times smaller than the time duration  $T_{90}$ . Therefore, the  $\tau$  time-scale is in most cases well sampled, and it is not significantly affected by the limited burst duration. Furthermore, it directly relates to the observed low-frequency break in the typical power-law behavior found in power density spectra analysis (Beloborodov et al. 2000).

In order to investigate the generality of the self-similarity in equation (4), we have subdivided our sample, for examples, in halves of high and low values of  $T_{90}$ . The same self-similar structure is found in the subsamples, and the same relation between the temporal variables is derived when performing separated PCAs, although with lower statistical significance due to the smaller number of sources in each subset.

In Figure 2 we show a scatter plot of equation (4). Considering that the coefficient associated with the variability  $V$  in  $PC_{10}$  has a small but non-negligible value (see Table 3), we indicate also in the figure the degree of variability  $V$  using a color scale, relating in this way all four temporal variables. The data points lie within a roughly angular sector where the lower limit is given approximately by the identity relation  $T_{50} \simeq \tau$  (dashed line). When fitting the data points using a power-law model (shown in solid line) we obtain an index  $0.60 \pm 0.03$  in agreement with equation (4). It is seen that bursts with low values of  $V$  (reddish points) have a distribution which differs significantly from those with high values (bluish points). Bursts with large values of  $V$  are mainly found well above the identity line and close to the upper-right vertex, while those with low values of  $V$  tend to lie closer to the identity line and at some distance from the vertex. Since the value of  $V$  is a measure of the complexity of the short time-scale structure in a given burst, this indicates that the distribution of  $V$ -values in Figure 2 could be due to a varying number of pulses (see also the discussion by Li & Paczyński 2006,

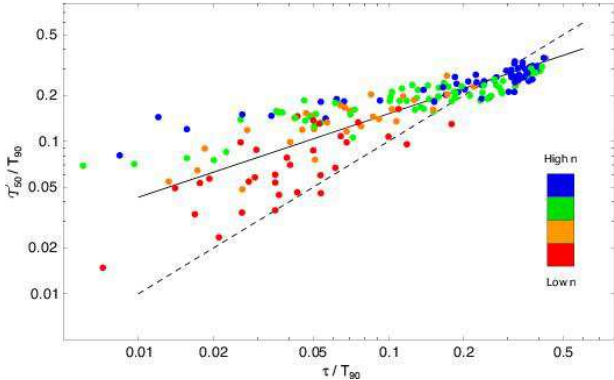


FIG. 3.— Synthetic data points based on artificial burst light curves. A simple *toy model* is used to generate light curves with a random number of exponential pulses (see text for details). The range and distribution of the data points are well matched with those in Figure 2 for  $n_{\max} = 25$  and a power-law fit (*solid line*) gives an index  $0.58 \pm 0.03$  in agreement with equation (4) within uncertainties. The color scale indicates the number of pulses. Bursts with few pulses (*red points*) lie close to the identity relation (*dashed line*), while bursts with a larger number of pulses lie further from this line (*orange-green points*). As overlap becomes increasingly important (*green-blue points*) in bursts with a large number of pulses, they move towards the upper-right vertex. In Figure 2 the regions of high and low variability  $V$  follow the same behavior pattern, indicating that  $V$  is an indirect measure of the number of pulses.

on the connection between the value of  $V$  and the number of pulses).

In order to test this idea we proceeded to reproduce the observations using synthetic burst light curves based on a *toy model* that generates a random number of exponential pulses. We found that the qualitative behavior does not depend on the pulse shape. To minimize the number of free parameters we fixed the pulse amplitudes and the burst duration  $T_{90}$ , the latter motivated by the observed self-similar structure of the bursts. We adopted a normal distribution for the decay characteristic times  $t_d$ . The parameters of the  $t_d$  distribution (i.e., its mean value and dispersion) are basically set by those of the observed  $\tau$ -distribution since  $t_d \sim \tau$ . Furthermore, a uniform probability distribution  $U[1, n_{\max}]$  was assumed for the number of pulses. Values for  $t_d$  and the number of pulses were chosen randomly from their assumed distributions. Bursts were then generated by placing the pulses randomly within the time span  $T_{90}$ . We adjusted the only free parameter  $n_{\max}$  in order to approximately reproduce the range of values, means, and dispersions observed in the  $T_{50}$  ordinate, and to obtain a power-law fit with index  $\sim 0.6$  as in equation (4).

The best match was found using a pulse distribution with  $n_{\max} \sim 25$ . With this simple model we were able to reproduce all the main features observed in Figure 2. An example of a good match between the outcome of our simulations and the observations is shown in Figure 3, where the color scale now corresponds to the number of pulses. Single-pulse bursts are found close to the identity line because in those cases  $T_{50} \simeq \tau \sim t_d$ . Bursts whose light curves have a few well-separated pulses lie above the line since for uncorrelated random pulses  $\tau$  will be approximately the same as for a single pulse, while the emission time  $T_{50}$  will increase (*red and orange points*). The chance of pulse overlap grows with the number of pulses, and as they start to overlap a shift towards larger  $\tau$ -values occurs and, hence, both  $\tau$  and  $T_{50}$  increase. Finally, bursts showing many heavily overlapping pulses resemble a single broad pulse and these will populate the upper-

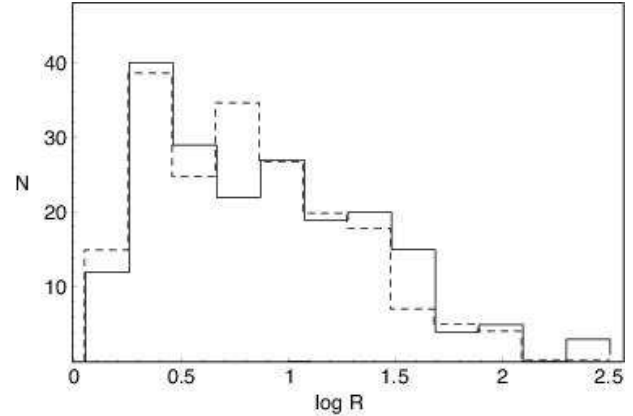


FIG. 4.— Analysis of the data-point distribution in Figure 2 taken the radial distance  $R$  from the upper-right vertex as reference. On the log-linear histogram representation the density decrease is approximately linear (*solid lines*). Bursts with heavily overlapping pulses lie near the vertex at small radii, where the relation between  $T_{50}$  and  $\tau$  “saturates” (see text). The distribution for the synthetic data in Figure 3 is shown for comparison (*dashed lines*). Based on the K-S test the differences between the two distributions are not significant.

right vertex (*green and blue points*). In Figure 2 the regions of high and low variability,  $V$ , follow the same behavior pattern, indicating that  $V$  is an indirect measure of the number of pulses. The bursts with low values of  $V$  at the upper-right vertex would then correspond to light curves with a large number of pulses so that the pulse overlap is large enough to resemble a single pulse. A complementary way of comparing observations with simulations is used in Figure 4, which shows the radial distribution of points taken the upper-right vertex as reference.

The main features of this toy model rely on the self-similar characteristics of the statistical properties of  $\tau$  and  $T_{50}$  (i.e., their mean values and dispersions scale with  $T_{90}$ ). This implies that significant overlap of pulses start to occur when the number of pulses is  $n_o$ , where  $n_o \propto (\tau/T_{90})^{-1/2}$  (assuming  $n_o \gg 1$ ). The value of  $T_{50}$  at this point is, roughly,  $n_o \tau$ , or  $T_{50} \propto \tau^{1/2}$ . This power-law index in the relation between  $T_{50}$  and  $\tau$  is smaller than the observed one ( $\approx 0.6$ ), indicating that overlap of pulses is more significant for larger values of  $\tau/T_{90}$ . In the toy model this is achieved by assuming  $n_{\max}$  to be independent of  $\tau/T_{90}$ . This is a non-trivial aspect of the toy model, since this independency together with the actual value of  $n_{\max}$  are both needed in order to account for the two independent characteristics of the observed relation between  $T_{50}$  and  $\tau$ , namely, the power-law index and the radial distribution shown in Figure 4.

## 5.2. $E_{\text{pk}}\text{-}\mathcal{F}\text{-}\tau$ Correlation

The ninth PC has also a small associated variation ( $\text{Var} \simeq 2.1\%$ ), and disregarding small loadings as before, it can be interpreted as a fairly constant relation between  $\mathcal{F}$ ,  $E_{\text{pk}}$ , and  $\tau$ . Since the correlations of  $T_{50}$  with the first two variables are the same as the corresponding ones with  $\tau$ , some degeneracy between the two temporal variables could have been expected. However, the associated uncertainties are not particularly large which indicates that, in the context of this 10-dimensional multivariate analysis, it is  $\tau$  that best maximizes the variance of  $PC_9$ . On the other hand, doing the PCA with only three variables gives almost identical results using either  $\tau$  or  $T_{50}$ . The relation between the three original variables can

be approximately written as

$$E_{\text{pk}} \propto \mathcal{F}^{0.8} \tau^{-0.6}, \quad (5)$$

where the reported exponents have been derived from a PCA restricted to the three-variable subset. They are a more adequate reference for the numerical simulation that will be presented below, which is limited to the same subspace. In any case, the index values in equation (5) are equal within uncertainties to the ones that are obtained from Tables 2 and 3.

The fact that the strength of the correlation between  $E_{\text{pk}}$  and  $\mathcal{F}$  is increased by an additional temporal variable is particularly interesting, since an analogous behavior has been observed in the study of the corresponding local frame variables. Amati et al. (2002) found that in the local frame  $E'_{\text{pk}} \propto E'_{\text{iso}}^{0.52 \pm 0.06}$ , where  $E_{\text{iso}}$  is the isotropic equivalent gamma-ray energy. It was later shown by Ghirlanda et al. (2004) that the scatter around this relation derived mainly from different values of the break time,  $t'_b$ , as measured in the afterglow light curves. This suggests a relation between characteristic time-scales in the prompt emission ( $\tau$ ) and in the afterglow ( $t'_b$ ). An additional thing to note from equation (5) is the exponent of  $\mathcal{F}$ , which differs markedly from the one deduced above from the bivariate correlation, namely  $E_{\text{pk}} \propto \mathcal{F}^{0.29 \pm 0.03}$ . This illustrates the fact that projection effects can strongly influence the deduced relation between observables.

The observed relation between  $E_{\text{pk}}$ ,  $\mathcal{F}$ , and  $\tau$  in equation (5) as well as the observed variance are affected both by the unknown redshifts and the sample selection criteria. Hence, the usefulness of equation (5) depends critically on the possibility to account for these effects. To this end, we assume a local frame relation of the form

$$E'_{\text{pk}} \propto E'_{\text{iso}}^a \tau'^b, \quad (6)$$

for which we like to determine values of  $a$  and  $b$  consistent with observations. Since the inversion problem has no unique solution under the present conditions, the use of Monte Carlo methods together with a forward-folding technique seems to be the best way to constrain the  $\{a, b\}$  parameter space. Restricting the PCA to a 3-dimensional subset, the third PC gives the relation shown in equation (5), but with a higher associated eigenvalue of 7.7% since now this percentage is taken over a smaller total variation (i.e., from Table 3, approximately 10/3 times 2.1%). We will assume that all source and observer's frame variables have log-normal distributions and therefore are fully determined by their means and standard deviations.

In principle, the PCA can be used to simulate any correlation matrix for the synthetic data, generating first random realizations of the uncorrelated PCs and then transform them to the original variables using the matrix of eigenvectors. However, in this way it is difficult to explore systematically the parameter space  $\{a, b\}$ , since these parameters can not be used as starting conditions. Initially, we tried this general approach but only to verify that  $E'_{\text{pk}}$  and  $\tau'$  can be assumed uncorrelated, and a simpler procedure was then used for our problem.

We proceeded instead by estimating values for the parameters of the probability distributions of  $E'_{\text{pk}}$  and  $\tau'$  and used these to generate random values. The  $E_{\text{iso}}$ -value is then derived using equation (6) for a given  $(a_i, b_i)$  pair. In this way we are exploiting also the fact that  $E_{\text{iso}}$  has the largest dispersion. It is assumed that the rest-frame relation in equation (6) has no intrinsic variance, i.e., that  $E_{\text{iso}}$ ,  $E'_{\text{pk}}$ , and  $\tau'$  lie strictly in a plane. Since the observed variance in equation (5) is a con-

volution of the intrinsic variance and that introduced by unknown redshift and selection criteria, the derived variance is a lower limit. Hence, acceptable values for  $\{a, b\}$  are those that in addition to reproducing equation (5), also have a variance not larger than the observed one. Next, we convert the data to the observer's frame. To do so, we estimate the redshift distribution from the pre-*Swift* sample of known redshifts. The conversion  $\mathcal{F} = E_{\text{iso}}(1+z)/(4\pi d_L^2)$  involves the luminosity distance  $d_L(z)$ , which depends on cosmological parameters. We adopt current standard values with a Hubble constant  $H_0 = 65 \text{ km s}^{-1} \text{ Mpc}^{-1}$ , a matter density  $\Omega_m = 0.3$ , and a vacuum energy density  $\Omega_\Lambda = 0.7$ . We also consider  $E_{\text{iso}}$ ,  $E'_{\text{pk}}$ , and  $\tau'$  redshift independent (i.e., evolution effects are neglected).

The simulated data point  $(\mathcal{F}, E_{\text{pk}}, \tau)_j$  thus obtained is then accepted as an observation or rejected according to the observational constraints of our sample data and the sample selection criteria (see § 2.1). The BATSE energy window is much wider than the observed  $E_{\text{pk}}$  distribution, so the selection is not very sensitive to its effective limits. However, the treatment of the flux selection criterium is less straightforward, since a value for the flux is not directly available in our simulations. Hence, the flux selection criterium has to be translated into a criterium relevant for the parameters in the simulations. In a bivariate correlation analysis between the flux  $F_{1s}$  and each one of our variables, only the fluence  $\mathcal{F}$  seems to have a significant correlation with  $R_{[\log F_{1s}, \log \mathcal{F}]} = 0.56$ . However, a multivariate PCA involving the flux and the three parameters under study reveals a well-defined thin correlation-plane in the  $\{F_{1s}, \mathcal{F}, \tau\}$  parameter subspace (with associated eigenvalue 2%). Note that we do observe a correlation between  $\mathcal{F}$  and  $\tau$  (Table 2), but we found a negligibly small  $R$ -value between  $F_{1s}$  and  $\tau$ . This illustrates that in general, when dealing with real experimental data, the measure of correlation  $R$  does not necessarily show the transitive property. It is also a good example of the robustness of the multivariate method discussed before in § 5. The intersection of the  $\{F_{1s}, \mathcal{F}, \tau\}$  correlation-plane with the boundary-plane given by the selection criterion  $F_{1s} \geq 4 \text{ photons cm}^{-2} \text{s}^{-1}$  determines the threshold of acceptance. This can be approximately modelled using the inequality  $\log \mathcal{F} \gtrsim (-5.5 + \log \tau)$ .

After the acceptance test, the process is repeated until the number of data points equals the size of the sample (197). Then, means and standard deviations are calculated and compared with the observed values and the initial parameters of the local distributions of variables are corrected accordingly in an iterative cycle until the calculated values agree with the observed ones. By this method our estimation of the  $E_{\text{iso}}$  dispersion is consistent with the ones based on the few GRBs with known redshifts (Frail et al. 2001; Ghirlanda et al. 2004).

Once the appropriate distribution parameters for the local variables are estimated, it is straightforward to generate many fiducial  $(\mathcal{F}, E_{\text{pk}}, \tau)$  sets. We then apply the PCA to each set and calculate means and standard deviations of the eigenvectors and eigenvalues. In particular, the values associated with the third PC (i.e., the last PC in this three variables PCA) are compared to the observed relation (eq. [5]). If they agree within uncertainties, then the initial values  $(a_i, b_i)$  are accepted as compatible with the observations. Values of  $(a_i, b_i)$  consistent with equation (5) are shown in Figure 5 together with the associated eigenvalues (variances).

As mentioned above, valid eigenvalues should not be larger than the observed value  $(7.7 \pm 0.7)\%$  within uncertainties (approximately 10% of the reported values). As can be seen from

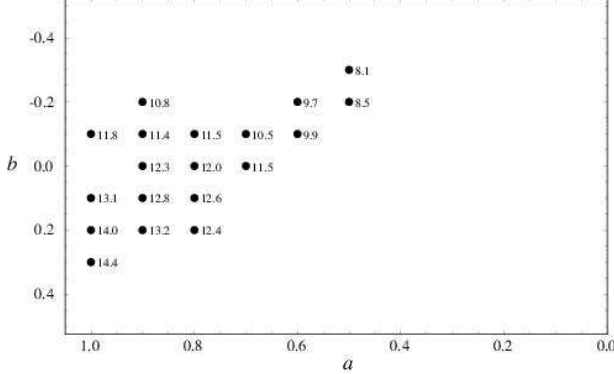


FIG. 5.— Parameter space of the power-law indices  $\{a, b\}$  in the relation  $E'_{\text{pk}} \propto E_{\text{iso}}^a \tau'^b$ . The dots indicate values compatible with the observations (i.e., eq.[ 5]), and they are labelled with the corresponding PCA eigenvalues that represent the percentage of the total variation. The best match with the observed eigenvalue  $(7.7 \pm 0.7)\%$  is  $(8.1 \pm 0.8)\%$  which corresponds to  $(a, b) = (0.5, -0.3)$ .

Figure 5, in all cases the calculated eigenvalues are equal to or larger than the observed ones, which implies: 1) Acceptable values of  $\{a, b\}$  lie within a small region of parameter space, and 2) the intrinsic variance in the relation between  $E_{\text{iso}}$ ,  $E'_{\text{pk}}$ , and  $\tau'$  is considerably smaller than the observed one, which is then mainly due to unknown redshifts and the sample selection criterium.

The above conclusions regarding the intrinsic properties of the relation in equation (6) are quite restrictive. However, they do rely on the validity of our treatment of unknown redshifts and sample selection criteria. We now discuss these aspects in turn. It could be argued that the set of pre-*Swift* GRBs with known redshifts  $z$  used above is not representative of the whole BATSE sample of long GRBs, since the determination of  $z$  always involved the more precise localization provided by other instruments with different trigger criteria and lower sensitivities. However, it has been shown by statistical analysis of the distributions of physical parameters that there are no significant differences between that set and the set of long *bright* BATSE bursts (Bosnjak et al. 2005), which are the ones considered in this work. In order to directly investigate the influence of the redshift distribution on our results, a broader redshift distribution that peaks at  $z \approx 2$  (i.e., about twice the  $z$  mean value and dispersion observed by pre-*Swift* instruments) was assumed. This gave very similar results to those presented in Figure 5, although with somewhat larger uncertainties associated with the eigenvalues. Hence, the main conclusions of our analysis are not very sensitive to the assumed redshift distribution. Furthermore, among the different possible sample biases, we found the empirical modeling of the selection effect created by the correlation plane  $\{F_{1s}, \mathcal{F}, \tau\}$  to be the only relevant one. However, for reasonable choices of the threshold  $\mathcal{F}(\tau)$ , we found small variations in the index  $b$  and, in particular, a value significantly larger than zero. We therefore conclude that  $b = 0$  can be rejected and, hence, that a significant fraction of the scatter in the well-known  $E_{\text{iso}}-E'_{\text{pk}}$  relation must be due to variations in the value of  $\tau'$ . Our best-estimate values of the power-law indices in equation (6) are  $a = 0.50 \pm 0.05$  and  $b = -0.30 \pm 0.05$ . Note that the  $E_{\text{iso}}$  index is in agreement with Amati et al. (2002).

### 5.3. Correlation Structure

While the last PCs lead to direct functional dependencies between various variables, the first few PCs instead reflect global properties in that sub-sets of variables are identified which are more strongly interlinked with each other than with the rest. If all the variables were equally contributing to the first PC, it would have approximately equal coefficients or *loadings*, i.e., considering the normalization for  $n = 10$ , each  $PC_1$  coefficient would be  $\approx 0.32$ . Instead, for  $PC_1$  the loadings are dominated by the temporal parameters  $T_{90}$ ,  $T_{50}$ ,  $\tau$ , and to a lesser extent  $V$ . In  $PC_2$  we see roughly the complementary pattern, with significant loadings for the spectral group of variables, in particular  $E_{\text{pk}}$  and to a lesser extent  $\mathcal{RE}_{\text{pk}}$  and  $\alpha$ , but also  $\mathcal{S}_{\mathcal{F}}$ . The only parameter with significant loading in both of these PCs is  $\mathcal{F}$ . The vector  $PC_3$  is mainly driven by the two spectral evolution variables  $\tau_{\text{lag}}$  and  $\mathcal{RE}_{\text{pk}}$ . The variable  $V$  seems to contribute non-negligible loadings to all three PCs, although with somewhat lower significance for  $PC_2$  and  $PC_3$  due to the larger error bars. One may also note that the loadings for  $V$  occur with opposite signs to those of  $\mathcal{S}_{\mathcal{F}}$  and  $\mathcal{RE}_{\text{pk}}$ , indicating an anti-correlation. Since  $\mathcal{S}_{\mathcal{F}}$  is related to the FRED-like appearance of the burst, it was argued in § 4.2 that the degree of correlation between  $\mathcal{S}_{\mathcal{F}}$  and  $\mathcal{RE}_{\text{pk}}$  is a measure of the prominence of the hardness-intensity correlation in the burst. In the toy-model discussed in § 5.1,  $V$  is directly related to the number of pulses in the burst. Hence, if the hardness-intensity correlation as well as the FRED-like appearance are associated with the individual pulses rather than the burst itself, the fact that  $V$  anti-correlates with both  $\mathcal{S}_{\mathcal{F}}$  and  $\mathcal{RE}_{\text{pk}}$  could be attributed to the expected weakening of both these characteristics as the number of pulses increases.

One of the objectives of empirical methods like the multivariate correlation analysis is to reveal the multiple dependencies between the observed parameters. The PCs with the smallest and largest eigenvalues give complementary information regarding the statistical properties of the sample. However, such an analysis has many limitations; for example, one cannot tell whether a correlation that is found indicates a direct causal connection or just an association through some variable, not necessarily included in the analysis. In order to give a somewhat different view of the statistical properties of our sample of GRBs we tried various other methods. The simplest approach was to directly inspect the correlation matrix (Table 2), ranking the strongest correlations for each parameter. This method is illustrated in Figure 6a. If a given correlation is ranked high for two parameters it would indicate a close connection between them. However, this reciprocity is rare when dealing with a large number of variables and instead it is more likely to find, like in our case, subsets that are interlinked. The problem then is that one cannot distinguish between indirect and weak dependencies.

An intermediary method, which combines the ranking of correlations and the PCA, is to use the PCA to find the correlation between a given parameter and any number of the remaining parameters. The simplest version is to find three-parameter correlations and to derive relations like equation (5) where one of the parameters appears as a product of power-law functions of the other two. Hence, two parameters are used to form an estimator of the third and the best model is defined as that giving the largest correlation coefficient between predicted and actual value. On several numerical experiments with multiple intercorrelated random variables, this scheme was found useful to reveal which variables were more directly connected. A variety of functional dependencies were investigated, from simple “chain” structures (where one vari-

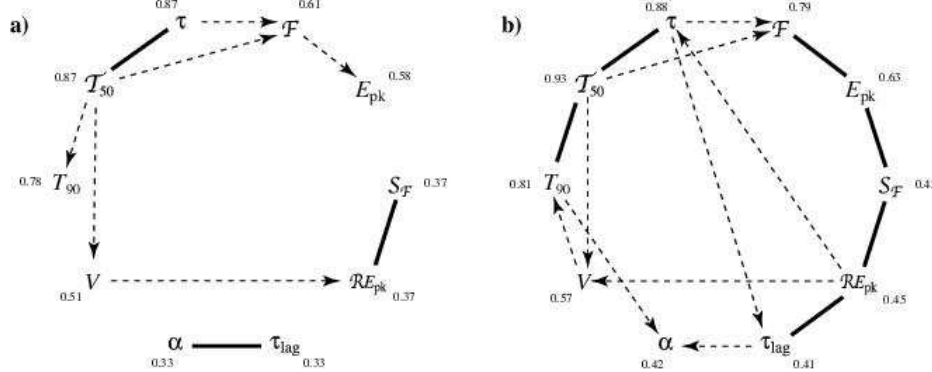


FIG. 6.— Schematic representation of the correlation structure for our set of 10 GRB parameters. Reciprocal relations suggest a close proximity between parameters (solid lines), while non-reciprocal relations indicate a correlation of lower significance (dotted lines with single arrows). (a) Each parameter is pointed at by the parameter(s) showing highest correlation with it, as given by Table 2. (b) We apply the PCA to all possible triad subsets and find for each parameter which other two are the best to construct an estimator. In the context of this analysis, for the fluence  $F$  equally good estimators can be derived using  $E_{\text{pk}}$  and either  $\tau$  or  $T_{50}$ . The numbers indicate the correlation coefficient  $R$  of each parameter with its corresponding two-parameters estimator.

able drives another that in turns drives another, and so forth) to more complex structures generated by multiple crossed assignments between the variables. Random noise was added at every instance to weaken the correlations. In all cases the PCA based method consistently produced better results than the direct reading of the correlation matrix (i.e., the two dimensional case). Under high noise levels the test produced less but rarely false identifications.

For each of the GRB parameters in our set of 10, we consider all possible three dimensional subsets and then calculate their PCs. In each case we derive a parameter estimator from the last PC (i.e., the one with the smallest eigenvalue) and calculate the corresponding correlation with the actual parameter. In this way we find for every parameter which other two produce the best estimator. The analysis is summarized by the graph shown in Figure 6b. Reciprocal relations are taken as evidence for a close association and the parameters are arranged accordingly. Non-reciprocal relations (also shown) indicate associations at a significantly lower level of confidence. The first to notice from the two graphs in Figure 6 is that the use of the PCA-method reveals considerably more structure than does the ranking of correlations. The two distinct subsets of parameters that are apparent in Figure 6b directly relate to the first three PCs. However, Figure 6b provides information in addition to that contained in the first PCs, since it explicitly shows the relationship between the variables within each of the two subsets and also, to some extent, the connection between the subsets. The subset of temporal parameters is equivalent to  $PC_1$ , while the parameters in  $PC_2$  and  $PC_3$  seem to be joined in the other subset indicating a close connection between them. It is seen from Table 3 that the eigenvalues for  $PC_2$  and  $PC_3$  are rather similar and have values roughly half of that for  $PC_1$ . This suggests that although the spectral evolution is related to the overall spectral properties, it has its own distinctive features. Two additional things to notice from Figure 6b is that  $S_F$  belongs to the second subset of parameters and that  $V$  appears to have no strong relation to either of the two distinct subsets. This argues that not only the FRED-like structure but also the basic temporal and spectral properties are associated with the individual pulses. The overall properties of the burst is then determined mainly by the number of pulses.

## 6. DISCUSSION

The statistical properties of a sample of GRBs have been analyzed with the use of ten parameters chosen to bring forth the main characteristics as observed by BATSE. In a multivariate analysis it was found that  $\sim 70\%$  of the total variation in parameter values is driven by only three principal components. Half of that is due to temporal variations while the other half is roughly divided equally between two principal components describing, respectively, the average spectral properties and spectral evolution. A more refined analysis reveals that the parameters in the latter two principal components are closely related. Together with the similarity of the variance (eigenvalue) of these principal components, this makes it likely that the two principal components needed to describe the spectral variations are not uniquely defined by the present analysis. Hence, the conclusion is that there exist two distinct sub-groups of inter-related parameters, which describe the temporal and spectral properties, respectively, of GRBs. One may note from Figure 6b that the only parameter showing substantial connection to both sub-groups appears to be the fluence, i.e., its value is determined jointly by the two sub-groups.

Complementary information is provided by the principal components with the smallest variance. Since these directions in parameter space are defined by their narrow distributions of parameter values, they directly provide analytical relations between the parameters involved. It was found that the parameters in the temporal sub-group discussed above also obey such a well defined relation. It is noteworthy that this relation is self-similar in the sense that the mean values and dispersions of both the emission time ( $T_{50}$ ) and half-width of the autocorrelation function ( $\tau$ ) scale with the duration of the burst ( $T_{90}$ ). Since this relation is unaffected by the unknown redshifts, it is a characteristic intrinsic to the light curves of GRBs. It is seen from Figure 6b that the parameter  $V$ , which measures the small time-scale variability, is the only one (possibly also  $\alpha$ ) without any obvious connection to either of the two sub-groups. It was shown in § 5.1 that the observed relation between  $T_{50}$  and  $\tau$  finds a ready explanation in a toy model where the value of  $V$  is determined by the number of pulses in a burst. This implies that the scaling of  $T_{50}$  with  $T_{90}$  would be the same as that for  $\tau$  and, hence, the fundamental scaling is that between  $\tau$  and  $T_{90}$ .

Burst light curves have very diverse morphologies and it has been suggested (see, e.g., Golenetskii et al. 1983;

Borgonovo & Ryde 2001) that they are a composite of pulses, with each pulse representing a single physical event (e.g., in the internal shock scenario, collisions between shells). In the toy model, the number of pulses in a burst is measured by the value of  $V$ . Independent support for such an interpretation comes from the prominence of the hardness-intensity correlation. It is well-known that this correlation is most apparent in FRED-like bursts. This association is most clearly seen in our data when these are represented as in Figure 6b (i.e., the close relation between  $\mathcal{S}_F$  and  $\mathcal{R}E_{\text{pk}}$ ). The effects of  $V$  can best be seen in the PCs with the largest variances; in all three,  $V$  anti-correlates with both  $\mathcal{S}_F$  and  $\mathcal{R}E_{\text{pk}}$ , indicating that large values of  $V$  tend to smear out both the FRED-like structure and the hardness-intensity correlation. Hence, a simple interpretation of the data is that not only the self-similarity of the light curves but also the hardness-intensity correlation and the FRED-like structure are properties associated with the individual pulses and that the overall properties of a burst is determined by the number of pulses.

The correlation between fluence ( $\mathcal{F}$ ) and peak energy ( $E_{\text{pk}}$ ) was one of the first to be well established for GRBs. Subsequent analysis indicated that the scatter around this relation could be reduced if a time variable were included, although it remained unclear which time variable gave the best result. Part of the problem, when trying to make more quantitative estimates, was the lack of redshifts. With the use of a small sample of GRBs with known redshifts, Amati et al. (2002) found the rest-frame equivalent of the  $\mathcal{F}$ - $E_{\text{pk}}$ -relation (i.e., the  $E_{\text{iso}}$ - $E'_{\text{pk}}$ -relation), while Ghirlanda et al. (2004) showed that the scatter around this relation could be substantially reduced if account were taken of the rest-frame break-time ( $t'_b$ ) in the light curve of the ensuing afterglow (see also Liang & Zhang 2005). It is interesting to note that the functional dependence between  $E_{\text{pk}}$  and  $E_{\text{iso}}$  is the same in the Amati and Ghirlanda relations. This is due to the fact that the values of  $t'_b$  and  $E'_{\text{pk}}$  are uncorrelated. The reduction of the scatter in the Amati-relation with the use of a time-scale associated with the afterglow rather than the prompt emission indicates a close connection between these two phases.

Although the lack of redshifts prevents a determination of the relation between the values of  $E_{\text{iso}}$  and  $E'_{\text{pk}}$  for individual GRBs observed by BATSE, we have developed a method by which this relation can be investigated statistically for the sample as a whole from the observed  $E_{\text{pk}}$ - $\mathcal{F}$ - $\tau$  correlation. By matching both the mean values and the dispersions of these observables, we show that the Amati-relation can be derived from our sample of GRBs. Furthermore, the scatter around this relation correlates with the value of  $\tau'$ , the rest-frame value of the half-width of the autocorrelation function. This is analogous to the findings of Ghirlanda et al. (2004) that the scatter in the Amati-relation correlates with  $t'_b$ . The observed scatter in the  $E_{\text{pk}}$ - $\mathcal{F}$ - $\tau$  correlation is consistent with that expected from the unknown redshifts, indicating a small intrinsic scatter. During the prompt phase of a GRB, it is likely that the observer sees only a small portion of the jet; hence,  $\tau'$  measures a local property and its value could, in principle, vary over the jet (i.e., for different lines of sight). The value of  $t'_b$ , on the other hand, is due to the overall properties of the jet. The fact that both  $\tau'$  and  $t'_b$  reduce the scatter in the Amati-relation indicates that at least some of the local properties do not vary much over the jet.

Nakar & Piran (2005) and Band & Preece (2005) have argued that the Amati-relation is not consistent with the BATSE

data and may be the result of a selection effect. However, as shown here, the Amati-relation can, in fact, be derived from our sample of GRBs selected from the BATSE data. This is a complete, flux limited sample, which suggests that the Amati-relation is valid for the intrinsically most luminous GRBs. These apparently contradicting results may be caused by a double bias against observing afterglows with large values of  $t'_b$ : (1) Due to the anti-correlation between  $t'_b$  and  $E_{\text{iso}}$  found by Ghirlanda et al. (2004), afterglows with large values of  $t'_b$  are intrinsically weak. (2) The decline of the light curve with time makes it increasingly hard to establish a value for  $t'_b$  in those afterglows where the break occurs late. Hence, the inconsistency found by Nakar & Piran (2005) and Band & Preece (2005) could be due to a larger number of GRBs in the BATSE sample than assumed by them for which it is observationally hard to measure a break in the light curve of the afterglow. The Amati-relation would then constitute an upper envelope of a continuous distribution, a possibility also discussed by Nakar & Piran (2005). As a result, associating the break in the light curve with the opening angle of a jet, implies an average opening angle considerably larger than typically deduced from observations.

Firmani et al. (2006) have analyzed a sample of 15 GRBs with known redshifts and found a good correlation between peak luminosity ( $L_{\text{iso}}$ ),  $E'_{\text{pk}}$  and  $\mathcal{T}'_{50}$  (actually, they used  $\mathcal{T}'_{45}$  instead of  $\mathcal{T}'_{50}$ ). They argue that this is a correlation independent from the one between  $E_{\text{iso}}$ - $E'_{\text{pk}}$ - $t'_b$  on the ground that the scatter in the former correlation increases if  $t'_b$  is used instead of  $\mathcal{T}'_{50}$  as the third observable. This raises the question whether  $\mathcal{T}'_{50}$  and  $t'_b$  are both related to a third time-scale, not included in the analysis, which could then be the appropriate one to use in both of these correlations. If this were the case, the apparent independency would have no physical ground but due to a too limited analysis. Since we have used peak flux to select our sample, this observable (and, hence,  $L_{\text{iso}}$ ) was not included in the analysis. However, a few of our results have bearing on the relevance of the various time-scales. Although there is a strong correlation between  $\tau$  and  $\mathcal{T}_{50}$ , the full 10-parameter analysis clearly indicates that  $\tau$  is the preferred third observable rather than  $\mathcal{T}_{50}$  in the  $E_{\text{pk}}$ - $\mathcal{F}$ -relation. This is in contrast to a limited 3-parameter analysis which makes no difference between  $\tau$  and  $\mathcal{T}_{50}$ . Hence, averaging over (or excluding) parameters which contribute only a small amount to a given correlation, can smear out the distinction between direct and indirect dependencies. Furthermore, before applying our method to account for the effects of the unknown redshifts to the  $E_{\text{pk}}$ - $\mathcal{F}$ - $\tau$  correlation, we took some care to establish that the observed correlation between  $E_{\text{pk}}$  and  $\tau$  is consistent with being due to the unknown redshifts, i.e., that there is no intrinsic correlation between  $E'_{\text{pk}}$  and  $\tau'$ . As noted by Firmani et al. (2006), their low value for the sum of residuals  $\chi^2_r$  could be due to a correlation between the errors. In fact, in their sample the value of  $E'_{\text{pk}}$  correlates with that for  $\mathcal{T}'_{50}$ , indicating that an observable more fundamental than  $\mathcal{T}'_{50}$  may exist (note that the values of  $E'_{\text{pk}}$  and  $t'_b$  are uncorrelated). Given our analysis of the  $E_{\text{pk}}$ - $\mathcal{F}$ - $\tau$  relation, we suggest that this observable could be  $\tau'$ , which was not among the parameters considered by Firmani et al. (2006). It is then possible that  $\mathcal{T}'_{50}$  and  $t'_b$  are both related to  $\tau'$  and, hence, that  $E_{\text{iso}}$ - $E'_{\text{pk}}$ - $t'_b$  and  $L_{\text{iso}}$ - $E'_{\text{pk}}$ - $\mathcal{T}'_{50}$  are not independent correlations. In this context, one may note that in the toy model used above to account for several of the observed properties of GRBs,  $\tau'$  is the fundamental

TABLE 2  
CORRELATION MATRIX

Parameter	$\log T_{90}$	$\log T_{50}$	$\log \tau$	$\log V$	$\log \mathcal{S}_{\mathcal{F}}$	$\log \tau_{\text{lag}}$	$\log \mathcal{R}E_{\text{pk}}$	$\log \mathcal{F}$	$\log E_{\text{pk}}$	$\alpha$
$\log T_{90}$	1. $\pm$ 0	0.78 $\pm$ 0.03	0.58 $\pm$ 0.04	0.18 $\pm$ 0.07	-0.09 $\pm$ 0.06	-0.01 $\pm$ 0.06	-0.15 $\pm$ 0.06	0.50 $\pm$ 0.05	0.24 $\pm$ 0.06	-0.26 $\pm$ 0.07
$\log T_{50}$	0.78 $\pm$ 0.03	1. $\pm$ 0	0.87 $\pm$ 0.02	0.51 $\pm$ 0.05	-0.25 $\pm$ 0.07	0.09 $\pm$ 0.07	-0.21 $\pm$ 0.06	0.61 $\pm$ 0.04	0.14 $\pm$ 0.08	-0.16 $\pm$ 0.07
$\log \tau$	0.58 $\pm$ 0.04	0.87 $\pm$ 0.02	1. $\pm$ 0	0.40 $\pm$ 0.06	-0.24 $\pm$ 0.07	0.15 $\pm$ 0.07	-0.25 $\pm$ 0.06	0.61 $\pm$ 0.04	0.14 $\pm$ 0.08	-0.12 $\pm$ 0.07
$\log V$	0.18 $\pm$ 0.07	0.51 $\pm$ 0.05	0.40 $\pm$ 0.06	1. $\pm$ 0	-0.32 $\pm$ 0.07	-0.18 $\pm$ 0.08	-0.37 $\pm$ 0.05	0.33 $\pm$ 0.06	0.08 $\pm$ 0.08	-0.07 $\pm$ 0.08
$\log \mathcal{S}_{\mathcal{F}}$	-0.09 $\pm$ 0.06	-0.25 $\pm$ 0.07	-0.24 $\pm$ 0.07	-0.32 $\pm$ 0.07	1. $\pm$ 0	-0.03 $\pm$ 0.07	0.37 $\pm$ 0.07	-0.07 $\pm$ 0.08	0.23 $\pm$ 0.07	0.03 $\pm$ 0.06
$\log \tau_{\text{lag}}$	-0.01 $\pm$ 0.06	0.09 $\pm$ 0.07	0.15 $\pm$ 0.07	-0.18 $\pm$ 0.08	-0.03 $\pm$ 0.07	1. $\pm$ 0	0.24 $\pm$ 0.08	-0.04 $\pm$ 0.06	-0.28 $\pm$ 0.06	0.33 $\pm$ 0.09
$\log \mathcal{R}E_{\text{pk}}$	-0.15 $\pm$ 0.06	-0.21 $\pm$ 0.06	-0.25 $\pm$ 0.06	-0.37 $\pm$ 0.05	0.37 $\pm$ 0.07	0.24 $\pm$ 0.08	1. $\pm$ 0	-0.03 $\pm$ 0.07	0.04 $\pm$ 0.07	-0.01 $\pm$ 0.08
$\log \mathcal{F}$	0.50 $\pm$ 0.05	0.61 $\pm$ 0.04	0.61 $\pm$ 0.04	0.33 $\pm$ 0.06	-0.07 $\pm$ 0.08	-0.04 $\pm$ 0.06	-0.03 $\pm$ 0.07	1. $\pm$ 0	0.58 $\pm$ 0.04	-0.20 $\pm$ 0.07
$\log E_{\text{pk}}$	0.24 $\pm$ 0.06	0.14 $\pm$ 0.08	0.14 $\pm$ 0.08	0.08 $\pm$ 0.08	0.23 $\pm$ 0.07	-0.28 $\pm$ 0.06	0.04 $\pm$ 0.07	0.58 $\pm$ 0.04	1. $\pm$ 0	-0.28 $\pm$ 0.07
$\alpha$	-0.26 $\pm$ 0.07	-0.16 $\pm$ 0.07	-0.12 $\pm$ 0.07	-0.07 $\pm$ 0.08	0.03 $\pm$ 0.06	0.33 $\pm$ 0.09	-0.01 $\pm$ 0.08	-0.20 $\pm$ 0.07	-0.28 $\pm$ 0.07	1. $\pm$ 0

TABLE 3  
PRINCIPAL COMPONENTS

PCs	$\log T_{90}$	$\log T_{50}$	$\log \tau$	$\log V$	$\log \mathcal{S}_{\mathcal{F}}$	$\log \tau_{\text{lag}}$	$\log \mathcal{R}E_{\text{pk}}$	$\log \mathcal{F}$	$\log E_{\text{pk}}$	$\alpha$	Var %	CVar %
$PC_1$	-0.41 $\pm$ 0.02	-0.49 $\pm$ 0.01	-0.45 $\pm$ 0.02	-0.31 $\pm$ 0.03	0.17 $\pm$ 0.05	0.04 $\pm$ 0.05	0.18 $\pm$ 0.04	-0.41 $\pm$ 0.02	-0.20 $\pm$ 0.05	0.16 $\pm$ 0.05	35.6 $\pm$ 1.6	35.6 $\pm$ 1.6
$PC_2$	0.09 $\pm$ 0.08	-0.11 $\pm$ 0.08	-0.13 $\pm$ 0.09	-0.22 $\pm$ 0.11	0.48 $\pm$ 0.08	-0.27 $\pm$ 0.25	0.34 $\pm$ 0.16	0.25 $\pm$ 0.06	0.56 $\pm$ 0.09	-0.35 $\pm$ 0.14	17.4 $\pm$ 1.6	53.0 $\pm$ 5.1
$PC_3$	-0.17 $\pm$ 0.07	-0.18 $\pm$ 0.05	-0.21 $\pm$ 0.05	0.29 $\pm$ 0.11	-0.22 $\pm$ 0.19	-0.66 $\pm$ 0.10	-0.46 $\pm$ 0.17	-0.13 $\pm$ 0.11	0.09 $\pm$ 0.20	-0.29 $\pm$ 0.15	14.9 $\pm$ 1.4	67.8 $\pm$ 5.5
$PC_4$	-0.30 $\pm$ 0.14	-0.09 $\pm$ 0.07	-0.01 $\pm$ 0.06	0.33 $\pm$ 0.16	0.23 $\pm$ 0.20	-0.02 $\pm$ 0.11	-0.16 $\pm$ 0.17	0.28 $\pm$ 0.10	0.37 $\pm$ 0.12	0.71 $\pm$ 0.12	8.7 $\pm$ 0.8	76.6 $\pm$ 2.1
$PC_5$	0.43 $\pm$ 0.13	0.12 $\pm$ 0.08	0.06 $\pm$ 0.07	-0.27 $\pm$ 0.25	0.55 $\pm$ 0.19	-0.22 $\pm$ 0.13	-0.46 $\pm$ 0.17	-0.28 $\pm$ 0.11	-0.16 $\pm$ 0.17	0.23 $\pm$ 0.23	6.9 $\pm$ 0.8	83.5 $\pm$ 3.1
$PC_6$	-0.10 $\pm$ 0.19	0.18 $\pm$ 0.07	0.04 $\pm$ 0.10	0.64 $\pm$ 0.14	0.45 $\pm$ 0.22	-0.14 $\pm$ 0.16	0.38 $\pm$ 0.20	-0.18 $\pm$ 0.13	-0.36 $\pm$ 0.12	-0.12 $\pm$ 0.20	6.1 $\pm$ 0.8	89.6 $\pm$ 2.9
$PC_7$	-0.32 $\pm$ 0.16	-0.12 $\pm$ 0.06	0.16 $\pm$ 0.17	0.12 $\pm$ 0.19	0.33 $\pm$ 0.16	0.55 $\pm$ 0.13	-0.46 $\pm$ 0.13	-0.07 $\pm$ 0.13	0.14 $\pm$ 0.15	-0.44 $\pm$ 0.10	4.5 $\pm$ 0.5	94.0 $\pm$ 1.1
$PC_8$	0.52 $\pm$ 0.11	-0.03 $\pm$ 0.06	-0.58 $\pm$ 0.09	0.36 $\pm$ 0.10	-0.09 $\pm$ 0.13	0.33 $\pm$ 0.16	-0.01 $\pm$ 0.16	-0.25 $\pm$ 0.13	0.29 $\pm$ 0.11	0.02 $\pm$ 0.13	3.4 $\pm$ 0.3	97.4 $\pm$ 0.6
$PC_9$	0.11 $\pm$ 0.10	-0.15 $\pm$ 0.05	-0.42 $\pm$ 0.10	0.02 $\pm$ 0.08	0.13 $\pm$ 0.06	0.06 $\pm$ 0.09	-0.17 $\pm$ 0.07	0.70 $\pm$ 0.05	-0.49 $\pm$ 0.06	-0.08 $\pm$ 0.06	2.1 $\pm$ 0.2	99.5 $\pm$ 0.1
$PC_{10}$	0.36 $\pm$ 0.03	-0.79 $\pm$ 0.01	0.45 $\pm$ 0.03	0.19 $\pm$ 0.03	-0.02 $\pm$ 0.02	-0.01 $\pm$ 0.02	0.09 $\pm$ 0.02	0.01 $\pm$ 0.03	-0.06 $\pm$ 0.03	0.02 $\pm$ 0.02	0.5 $\pm$ 0.1	100. $\pm$ 0.

parameter, while the value of  $T'_{50}$  is derived from  $\tau'$  and the number of pulses.

This research was supported by a grant from the Swedish

Science Research Council. Use has been made of BATSE data obtained from the High Energy Astrophysics Science Archive Research Center (HEASARC), provided by NASA's Goddard Space Flight Center.

## REFERENCES

Amati, L., et al. 2002, A&A, 390, 81  
 Bagoly, Z., Mészáros, A., Horváth, I., Balázs, L. G., & Mészáros, P. 1998, ApJ, 498, 342  
 Balázs, L. G., Bagoly, Z., Horváth, I., Mészáros, A., & Mészáros, P. 2003, A&A, 401, 129  
 Band, D., et al. 1993, ApJ, 413, 281  
 Band, D. L., & Preece, R. D. 2005, ApJ, 627, 319  
 Beloborodov, A. M., Stern, B. E., & Svensson, R. 2000, ApJ, 535, 158  
 Borgonovo, L. 2004, A&A, 418, 487  
 Borgonovo, L., & Ryde, F. 2001, ApJ, 548, 770  
 Borošon, T. A., & Green, R. F. 1992, ApJS, 80, 109  
 Borošon, T. A. 2002, ApJ, 565, 78  
 Bosnjak, Z., Celotti, A., Longo, F., & Barbiellini, G. 2005, ArXiv Astrophysics e-prints, arXiv:astro-ph/0502185  
 Devore, J. L. 1982, Probability and Statistics for Engineering and the Sciences (1st ed.; Monterey: Brooks/Cole Publishing Company)  
 Fenimore, E. E., & Ramirez-Ruiz, E. 2000, ArXiv Astrophysics e-prints, arXiv:astro-ph/0004176  
 Firmani, C., Ghisellini, G., Avila-Reese, V., & Ghirlanda, G. 2006, MNRAS, 370, 185  
 Fishman, G. J., et al. 1989, in Proc. of the GRO Science Workshop, ed. W. N. Johnson, 2  
 Frail, D. A., et al. 2001, ApJ, 562, L55  
 Ghirlanda, G., Ghisellini, G., & Lazzati, D. 2004, ApJ, 616, 331  
 Golenetskii, S. V., Mazets, E. P., Aptekar, R. L., & Ilyinskii, V. N. 1983, Nature, 306, 451  
 Guidorzi, C., Frontera, F., Montanari, E., Rossi, F., Amati, L., Gomboc, A., Hurley, K., & Mundell, C. G. 2005, MNRAS, 363, 315  
 Jolliffe, I. T. 2002, Principal Component Analysis, (2nd ed.; New York: Springer)  
 Lazzati, D. 2002, MNRAS, 337, 1426  
 Lee, T. T., & Petrosian, V. 1997, ApJ, 474, 37  
 Li, L.-X., & Paczyński, B. 2006, MNRAS, 366, 219  
 Liang, E., & Zhang, B. 2005, ApJ, 633, 611  
 Lloyd, N. M., & Petrosian, V. 2000, ApJ, 543, 722  
 Lloyd, N. M., Petrosian, V., & Mallozzi, R. S. 2000, ApJ, 534, 227  
 Mallozzi, R. S., Paciesas, W. S., Pendleton, G. N., Briggs, M. S., Preece, R. D., Meegan, C. A., & Fishman, G. J. 1995, ApJ, 454, 597  
 Mitrofanov, I. G., et al. 1999, ApJ, 522, 1069  
 Mukherjee, S., Feigelson, E. D., Jogesh Babu, G., Murtagh, F., Fraley, C., & Raftery, A. 1998, ApJ, 508, 314  
 Nakar, E., & Piran, T. 2005, MNRAS, 360, L73  
 Norris, J. P. 2002, ApJ, 579, 386  
 Norris, J. P., Marani, G. F., & Bonnell, J. T. 2000, ApJ, 534, 248  
 Preece, R. D., Briggs, M. S., Mallozzi, R. S., Pendleton, G. N., Paciesas, W. S., & Band, D. L. 1998, ApJ, 506, L23  
 Preece, R. D., Briggs, M. S., Mallozzi, R. S., Pendleton, G. N., Paciesas, W. S., & Band, D. L. 2000, ApJS, 126, 19  
 Press, W. H., Teukolsky, S. A., Vetterling, W. T., & Flannery, B. P. 1992, Numerical Recipes in Fortran (2d ed.; Cambridge: Cambridge Univ. Press )  
 Reichart, D. E., Lamb, D. Q., Fenimore, E. E., Ramirez-Ruiz, E., Cline, T. L., & Hurley, K. 2001, ApJ, 552, 57  
 Rhoads, J. E. 1997, ApJ, 487, L1  
 Schaefer, B. E., Deng, M., & Band, D. L. 2001, ApJ, 563, L123